

Characterization of dust aggregates in the vicinity of the *Rosetta* spacecraft

C. Güttler,^{1★} P. H. Hasselmann,² Y. Li,³ M. Fulle,⁴ C. Tubiana,¹ G. Kovacs,¹ J. Agarwal,¹ H. Sierks,¹ S. Fornasier,² M. Hofmann,¹ P. Gutiérrez Marqués,¹ T. Ott,⁵ E. Drolshagen,⁵ I. Bertini,⁶ C. Barbieri,⁷ P. L. Lamy,⁸ R. Rodrigo,^{9,10} D. Koschny,¹¹ H. Rickman,^{12,13} M. F. A’Hearn,¹⁴ M. A. Barucci,² D. Bodewits,¹⁴ J.-L. Bertaux,¹⁵ S. Boudreault,¹ G. Cremonese,¹⁶ V. Da Deppo,¹⁷ B. Davidsson,¹⁸ S. Debei,¹⁹ M. De Cecco,²⁰ J. Deller,¹ B. Geiger,²¹ O. Groussin,²² P. J. Gutiérrez,²³ S. F. Hviid,²⁴ W.-H. Ip,^{25,3} L. Jorda,²² H. U. Keller,^{26,24} J. Knollenberg,²⁴ J. R. Kramm,¹ E. Kührt,²⁴ M. Küppers,²¹ L. M. Lara,²³ M. Lazzarin,⁷ J. J. López-Moreno,²³ F. Marzari,⁷ S. Mottola,²⁴ G. Naletto,^{27,6,17} N. Oklay,²⁴ M. Pajola,²⁸ X. Shi,¹ N. Thomas^{29,30} and J.-B. Vincent²⁴

Affiliations are listed at the end of the paper

Accepted 2017 July 3. Received 2017 June 30; in original form 2017 March 31

ABSTRACT

In a *Rosetta*/OSIRIS imaging activity in 2015 June, we have observed the dynamic motion of particles close to the spacecraft. Due to the focal setting of the OSIRIS wide angle camera, these particles were blurred, which can be used to measure their distances to the spacecraft. We detected 109 dust aggregates over a 130 min long sequence, and find that their sizes are around a millimetre and their distances cluster between 2 and 40 m from the spacecraft. Their number densities are about a factor 10 higher than expected for the overall coma and highly fluctuating. Their velocities are small compared to the spacecraft orbital motion and directed away from the spacecraft, towards the comet. From this we conclude that they have interacted with the spacecraft and assess three possible scenarios. In the likeliest of the three scenarios, centimetre-sized aggregates collide with the spacecraft and we would observe the fragments. Ablation of a dust layer on the spacecraft’s *z* panel (remote instrument viewing direction) when rotated towards the Sun is a reasonable alternative. We could also measure an acceleration for a subset of 18 aggregates, which is directed away from the Sun and can be explain by a rocket effect, which requires a minimum ice fraction of the order of 0.1 per cent.

Key words: techniques: image processing – comets: general – comets: individual: 67P/Churyumov-Gerasimenko.

1 INTRODUCTION

The *Rosetta* mission at comet 67P/Churyumov-Gerasimenko (hereafter 67P) was a unique opportunity to study cometary dust with its (changing) properties and dynamics. Three *in situ* instruments were dedicated to the study of individual dust particles that reach the spacecraft. Collected particles by COSIMA and MIDAS consolidate our understanding that most of these are loosely bound aggregates down to the smallest scale (Bentley et al. 2016; Langevin et al. 2016). The GIADA instrument measured velocities and masses

of aggregates arriving at the *Rosetta* spacecraft. While the bulk of the particles are consistent with the pebbles seen by COSIMA and MIDAS, a non-negligible minority shows an extremely low density of 1 kg m^{-3} compared to the canonic value of 1000 kg m^{-3} (Fulle et al. 2015). The authors of the study concluded that a fractal nature of these particles would naturally explain the low density as well as the observation that these particles come in showers, which would then be explained by charge disruption. One particle, which can formally be described as being fractal was reported by Mannel et al. (2016).

Individual particles are also observed with the OSIRIS cameras on *Rosetta*. The advantage here is that the aggregates are typically unaltered by the spacecraft environment and that multiple

* E-mail: guettlerc@mps.mpg.de

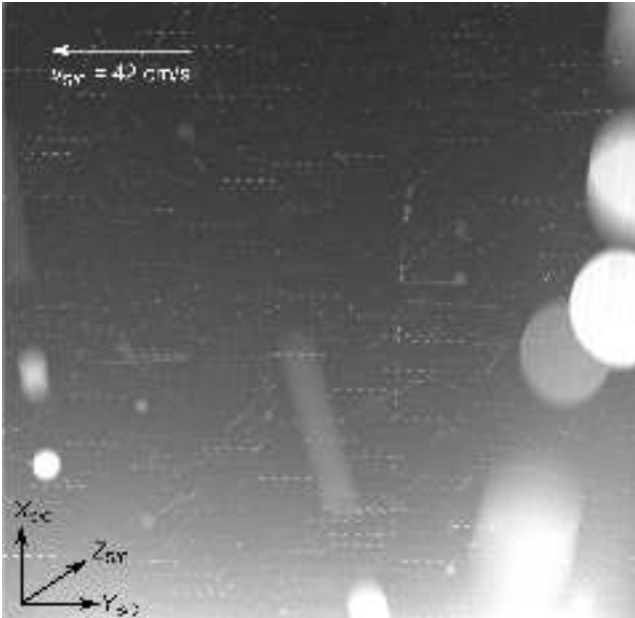


Figure 1. Stack of all images from the OSIRIS imaging sequence STP059_GRAIN_TRACK_001. Features, which appear very large are particles close to the camera. Many features appear as tracks on several images, while most horizontal tracks are star tracks due to a slow spacecraft rotation over the 130 min duration of the activity.

detections of a single particle can provide insight into their dynamics and – if performed in different bandpass filters – their colour and thus composition. The challenge for this remote sensing approach is to measure the aggregates’ distances from the spacecraft, which is needed to measure their sizes. There are several different approaches to measure the distance, which we will briefly summarize. Using the motion of the spacecraft and making the assumption that all particles are on radial trajectories away from the nucleus, Rotundi et al. (2015) and later Fulle et al. (2016) used the parallax to determine the distance. Combining these OSIRIS observations with GIADA detections, they presented a size distribution of particles in the coma, which is at the moment considered as the reference. In another approach, the parallax could be determined in a single observation, when both OSIRIS cameras [narrow angle camera (NAC) and wide angle camera (WAC)] are operated simultaneously. From the offset in the cameras’ optical axes, distances can be computed for particles within 6 km from the spacecraft. This method was applied by Ott et al. (2017) on 260 aggregates from 2015 June to September and their derived mass-loss rates are consistent with Fulle et al. (2016). A third method to constrain the distance is to make use of the knowledge of the aggregates’ dynamics. Agarwal et al. (2016) studied the trajectories of particles, close to the comet’s sub-solar limb. Aggregates, which are on a track directed away from the limb, have a high chance of just having left the comet, thus still being close to the comet where the distance is known.

A fourth approach to measure the distance of dust aggregates from the *Rosetta* spacecraft is presented in this study. If a particle is close to the camera, it will be out of focus and appear as an enlarged, featureless disc. If then the particle is small compared to the size of this apparent disc, the disc diameter is a direct measure of the distance. This study focuses on particles observed in the WAC, for which the furthest distance determination with this method is approx. 100 m. The analysed sequence is visualized in Fig. 1 and explained below.

It should be mentioned that this specific activity shows a high amount of dust, which is not seen at all times, thus not representative. This study is therefore aiming for a characterization of the dust with its physical parameters and processes. A broader analysis of more sequences of this type, including imagery of the NAC, is a natural extension of this work.

2 OBSERVATION AND DATA REDUCTION

2.1 Observation conditions

The OSIRIS science plan included regular imaging campaigns to study the dust-particle environment and allow the tracking of individual particles. In the frame of this paper, we have analysed one sequence with the name STP059_GRAIN_TRACK_001, which was run on the afternoon of 2015 June 6.¹ The activity contained 150 full-frame images taken in the red broad-band filter of the OSIRIS WAC with a field of view of 12° (Keller et al. 2007). We used triplets of exposure times (16, 4 and 1 s) with the intention of catching a wide range of slow, fast, bright and faint particles in the same sequence. The observation was grouped into five sets of 30 images each with 10 min duration and a gap of 20 min in-between. 15 images of the last two sets were acquired but never downloaded due to an overrun of the OSIRIS internal mass memory; thus, the total number of images reduces to 135. During the observation, the *Rosetta* spacecraft was 1.48 au from the Sun and 200 km from the comet with an orbit phase angle of 90°. The observation geometry was such that the *Rosetta* spacecraft was pointing 15° off the comet towards the sub-solar direction, resulting in an average phase angle of 105° for particles inside the WAC field of view. In this 12° field of view, particles at the top and bottom of the frame would be seen under a phase angle of 111° and 99°, respectively. The spacecraft pointing, thus field of view, was fixed in the comet frame such that stars appear trailed.

A stack of all images, where each pixel shows the maximum of the complete sequence, is displayed in Fig. 1. The orientation of the image is the standard orientation, where the spacecraft’s +y-axis (solar panel direction) is to the right and the spacecraft’s +x-axis is to the top. In this orientation, the comet is to the bottom of the frame, 9° off the image edge and the Sun is to the top. Due to the long exposure times, particles appear as elongated tracks and one can identify the triplets of exposures from the track length. The 16 s exposure was the first in each triplet, which allows a direct identification of the track direction (long–intermediate–short). Some of the features have a very large diameter, which is (as described above) not physical but an optical blur due to particles being close and out of the camera focus. The blur diameter can be directly translated into a particle’s distance from the camera as will be described below. Many parallel, horizontal tracks, split into five segments each, are visible, which are tracks of stars moving due to a small rotation of the spacecraft, which was tracking the comet. The displacement is 1.3 pixels per minute in the spacecraft –y direction, which is small against particle motions and therefore not corrected for in the analysis below. Narrow, unblurred tracks are particles far from the spacecraft.

2.2 Image analysis

Images were processed in a semi-automated manner with enough manual intervention to get precise and reliable results. The

¹ The data is available through the Planetary Science Archive of the European Space Agency under <https://www.cosmos.esa.int/web/psa/rosetta>

following steps were performed: All images were first filtered to achieve the best contrast over the full frame to allow a detection of the faintest possible features close to the noise limit. By means of custom software, each end of a particle trail was matched with a circle. The diameter of this circle could be different at the start and end position if the particle changed the distance to the spacecraft within the image exposure. The particle shape is characterized by the convex hull of these two circles and fully described by six parameters. The start and end position is only unique if a particle is detected in more than one image, otherwise the direction of motion is unknown. The direction is known for 84 out of 109 particles.

It should be noted that each single particle that was visible after the contrast enhancement was tracked in each possible image. So the data set is complete and can be used for a statistical interpretation below.

2.3 Particle distances

The distance of a dust particle with respect to the camera follows from the particle's blurring size and the knowledge of the camera's optical design (Keller et al. 2007). Using the ZEMAX OPTICSTUDIO software package, we performed simple paraxial calculations of ray-tracing test particles at different distances to the camera and measured their size on the CCD. The profiles of these blurred features are expected to be flat plateaus, which was confirmed in the images. As a reference point for the distance, we use the front of the camera baffle (i.e. the door location) throughout. The blur diameter D (in pixels) as a function of the object distance δ (in metres) was then fitted with a power law and we are using the inverse

$$\delta(D) = 356 \times \left(\frac{D}{\text{px}}\right)^{-1.13} \text{ m} \quad (1)$$

to compute the distance of blurred particles in our images. This relies on the assumption that particles are small enough to be unresolved, which will be verified below. For all particles, we calculate the distance for the start and the end position (which could be slightly different as previously described) in each image.

2.4 Photometry

For the photometry calculation of the particle tracks, we use OSIRIS level 3B images. These are radiometrically calibrated (spectral irradiance I) and geometric-distortion corrected images, normalized by the solar flux (spectral radiance F) at the heliocentric distance r_h of the observation, resulting in a reflectance $R = \pi I / (F_{\odot} / r_h^2)$ (for details see a description of the OSIRIS calibration in Tubiana et al. 2015).

A custom-designed photometric aperture method with a stadium geometry as an aperture was used and the optimum aperture verified through the growth-curve method. Technically, we used the line between a particle's start and end position measured above as an input (central red lines in Fig. 2), where a standard aperture method would have used a single point. This binary line was then dilated with discs of growing radii, which results in the geometric shape of a stadium (convex hull around two circles), used to mask the image.

The average background signal, calculated as the average from a stadium-shaped outline well outside the feature (size of outer shapes in Fig. 2), was computed and then removed from each pixel of the original image. This implies the assumption that the background signal is also added to the pixel area of the feature itself, which is reasonable since the feature is physically small compared to its blurred size on the CCD. Using this background corrected image,



Figure 2. Example of aperture photometry with stadium shape for three different particles. The central lines mark the position of the particle and the beginning of the aperture integration. The stadium shapes mark the mask where we measured the background signal.

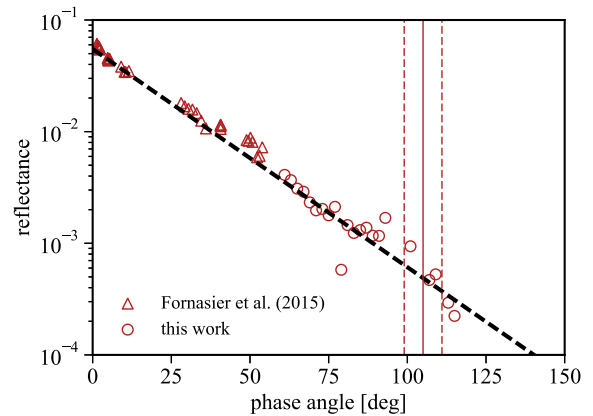


Figure 3. Nucleus phase function at 649.2 nm (orange filter) with data from Fornasier et al. (2015) (red triangles), extended in this work for larger phase angles (red circles; see Appendix A). The three vertical lines present the range (dashed) and average (solid) phase angle used for the dust observations below.

the feature signal (integrated reflectance) was computed by masking the image with growing stadium outlines and integrating these numbers. The integrated reflectance over growing radius must converge against a constant value outside the particle. This was manually verified for each case and we took the integral at a radius at 1.5 particle radii (determined as described in Section 2.2) as the particle's signal. Using OSIRIS level 3B images (reflectance) this integrated signal I_{dust} is an aggregate's integrated irradiance, but normalized by the solar flux as described above, which is convenient for the calculations below.

2.5 Phase function

As it will be confirmed below, the observed dust aggregates are macroscopic in that they are all larger than 0.3 mm in diameter (typically 1 mm). For the interpretation of their reflectance, we therefore treat them as reflecting surfaces. Although the aggregates might have been altered on their way from the comet to the spacecraft, the best assumption is still that they have the same photometric properties as the nucleus surface. This approximation is aided by the fact that 67P's surface is mostly single scattering and multiple scattering is expected to be negligible (Fornasier et al. 2015).

The phase function of 67P's surface is known from Fornasier et al. (2015) and plotted as reflectance in Fig. 3 (red triangles). The observations of dust aggregates in this work were all performed around 105° phase angle, which is not covered by the data of Fornasier et al. (2015). We therefore applied the same methodology as Fornasier et al. (2015) to OSIRIS imagery of the nucleus surface, in order to extend the data set to larger phase angles up to

115° (red circles). The method is described in Appendix A. The full data set (circles and triangles) was then fitted with an exponential function of the form

$$R_{67P}(\alpha) = 0.055 \times \exp(-0.045 \times \alpha), \quad (2)$$

which gives a value of $R_{67P}(\alpha = 105^\circ) = 4.9 \times 10^{-4}$ (dashed black line). The method applied by Fornasier et al. and in this work considers the integral reflectance per total observed area. This means that shadowed parts were included and the integral was normalized with respect to the total observed surface computed from synthetic images (Appendix A). As a result, equation (2) takes shadowing of dust aggregates due to their crescent shape and morphology already into account.

2.6 Physical aggregate size

The normalized integrated signal of the dust aggregates $R_{\text{dust}} = \pi I_{\text{dust}} / (F_{\odot} / r_h^2)$ can be translated into a physical size. If we divide it by the reflectance of comet 67P's surface R_{67P} at the same phase angle, we get the aggregate area in pixels if it was not blurred. Here we are using the comet's reflectance at a phase angle between 99° and 111°, depending on the measured CCD location of each individual particle detection, thus a particle's real phase angle at each time.

We find that 19 out of 109 particles have a theoretical area ($R_{\text{dust}} / R_{67P}$) larger than 1 pixel and only four of these have an area larger than 4 pixels. This theoretical area relates to the size of a particle as if it was in focus. The blurring method described above works best if this theoretical size of a particle is negligible compared to the blur size from the defocus. Only in that case the distance is purely determined by the blur diameter as assumed for equation (1). We find five particles showing an observed area (apparent size) of 10 pixels while all others are larger, i.e. 300 pixels in average. This is much larger than the theoretical area and thus the justification to use this method for distance determination for the particles studied in this article.

We can continue and translate the theoretical pixel area into a physical size, the aggregate radius a . With the known CCD pixel size of 13.5 μm (Keller et al. 2007) and the effective focal length of 136 mm (for geometrically corrected WAC images), we can write down

$$a = \frac{1}{\sqrt{\pi}} \sqrt{\frac{R_{\text{dust}}}{R_{67P}}} \times \frac{13.5 \mu\text{m}}{136 \text{ mm}} \times \delta. \quad (3)$$

The aggregate sizes from each detection of a particle, i.e. over time, were manually reviewed. They show some scatter due to the uncertainty of the distance but no overall trend. The median value from all detections therefore provides a robust measure for an aggregate's radius.

The result of the calculated particle sizes and distances is shown in Fig. 4. It is interesting to note in this context, that the detection limit is barely depending on the aggregate's distance. If an aggregate is closer to the spacecraft, its total signal is larger but as it is getting apparently bigger due to the blur, and its surface brightness is nearly constant [scaling with $\delta^{0.12}$, see equation (B6) in Appendix B]. A reasonable detection limit related to a signal of 15 digital numbers is plotted as the dashed line in Fig. 4 and is matching the expectations.

The figure shows a pronounced cluster of approx. millimetre-sized aggregates around 10 m from the spacecraft. There are a few centimetre-sized aggregates, but only for large distances of 50–100 m, i.e. inside a much larger sampling volume. Close aggregates

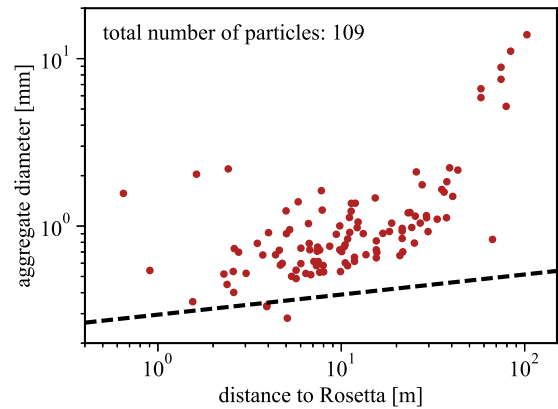


Figure 4. All aggregates with their diameter and distance to the spacecraft. The dashed line is an estimated detection limit derived in Appendix B, smaller particles would be too faint to detect.

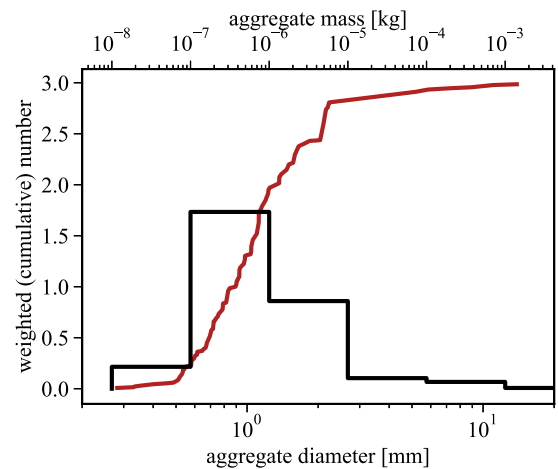


Figure 5. Cumulative (red curve) and histogram (black curve) size distribution of all particles in the analysed sequence.

of this size would be easily visible but are not present (no aggregates in top left corner of the plot).

There is also a population missing for small aggregates (approx. mm) at distances between 50 and 100 m. These are above the signal detection threshold, but would appear relatively small. Technically we used a blurring-diameter detection limit of 3 pixels (100 m), while the missing population would have diameters between 3 and 6 pixels.

3 RESULTS

3.1 Dust size distribution

The size distribution of 109 particles found in the sequence is presented in Fig. 5. Each aggregate is assigned a weighted number, which is the number of images it appears in, divided by the total number of images in the sequence. The weighted number was cumulated and plotted as a red solid line. As already noticed above, the median of the sizes is around a millimetre, the largest particles range up to a centimetre.

If we assume an aggregate mass density of 1000 kg m^{-3} (keeping consistency with Rotundi et al. 2015), we can translate the aggregate diameters into aggregate masses denoted on the upper axis. The black solid curve shows the same data as a histogram in

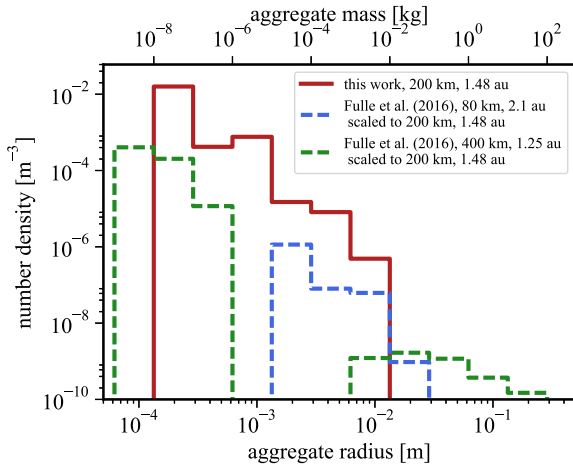


Figure 6. The number density of aggregates from this work (solid red line) compared to the previous study by Fulle et al. (2016) (blue and green dashed lines). For comparability, the data by Fulle et al. (2016) was scaled to our cometocentric and heliocentric distance.

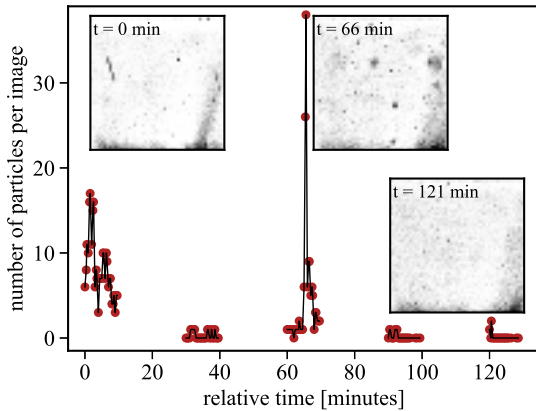


Figure 7. The number of particles close to the spacecraft is highly fluctuating over time. The burst at 66 min after the beginning of the sequence is very prominent.

logarithmic mass bins in decades of aggregate mass. The three mass bins between 10^{-5} and 10^{-2} kg contain only 1, 5 and 1 particles, which should be kept in mind for the statistical interpretation below.

We can convert our weighted numbers into a number density by dividing them by the observation volume, which has a pyramid shape where the camera looks from the apex. The height of the pyramid is in our case defined by the distance we see, for which we apply the distance of the furthest particle per bin. These data are shown as a red solid line in Fig. 6. In comparison, we show the size distribution measured by Fulle et al. (2016) at 1.25 and 2.1 au, both scaled to our cometocentric and heliocentric distance of 200 km and 1.48 au. We scale the number density with distance to the comet as r_c^{-2} and with heliocentric distance as $r_h^{-5.1}$ (scaling of the water production rate from Hansen et al. 2016). While the combined scaling factors for both cases are rather mild (0.69 and 1.97, respectively), the difference between our number densities and those measured by Fulle et al. (2016) account for a factor 10. Combining results of the *Rosetta* GIADA and OSIRIS instruments, the size distribution by Fulle et al. (2016) was determined from the GIADA flux (small particles) and a parallax method from OSIRIS imagery (large particles; cp. Section 1).

This number density is surprisingly high, but we have to point out that it is strongly fluctuating with time. Fig. 7 shows the number of

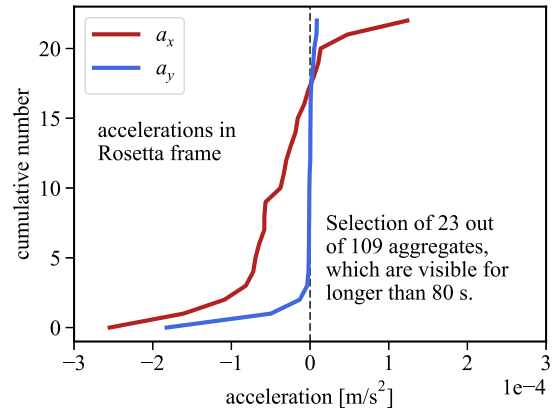
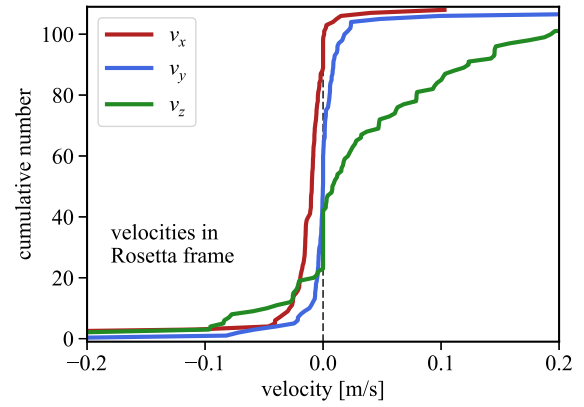


Figure 8. Velocity distribution of all particles (top) and the distribution of accelerations for a subset of particles, which were visible for longer than 80 s (bottom).

particles per image as a function of the time relative to the beginning of the observation sequence. While the number fluctuates around 10 particles per image in the beginning, it goes down to only a single particle per image 20 min later. After 66 min from the beginning of the sequence, a burst of more than 30 particles in a single image is very prominent, before they vanish within few minutes. The rest of the sequence is quiet again, the three insets provide a visual impression of the fluctuation for three representative times.

3.2 Particle motion

One advantage of this study is that we have precise trajectory information. The aggregate position on the camera CCD was determined as described above and then transformed into a metric, Cartesian coordinate system. To achieve this, the distance component z was linearly fitted, which was then used to correct the $x(t)$ and $y(t)$ components for the opening angle of the camera. These two components were then fitted with a second-order polynomial and each trajectory was manually reviewed. All x and y tracks were matching the fit to the limit of the small noise in measured position, while the fits in z direction possess an error of the order of 10–20 per cent for those tracks where the distance is actually changing.

The velocities are presented in Fig. 8 (top), where all three components are directed as visualized in Fig. 1 and the v_z component away from the spacecraft, roughly towards the comet. The v_y component of the velocity, marked by the blue line, has a clear median at 0 m s^{-1} and a width of the distribution of less than 1 cm s^{-1} . The v_x component of the velocity (red line) is slightly negative (approx. -1 cm s^{-1}), which means that it is directed downwards in Fig. 1

and, in the projection, away from the Sun, which is straight up in the image. It is noteworthy that the velocities were not corrected for the spacecraft motion, which was 42 cm s^{-1} towards the $-y$ direction. So we see aggregates, which move along with the spacecraft in the y direction and faster than the spacecraft in the anti-sun-ward $-x$ direction. The last component, the v_z velocity (green line) is positive for the large majority of aggregates, which is away from the spacecraft and roughly towards the comet, which direction is 15° inclined against z . Also this velocity is larger and shows a wider spread than the other two components.

The acceleration (again not spacecraft motion corrected, thus in the *Rosetta* frame) was determined only for a subset of 23 aggregates, which were observed long enough to make the acceleration measurable. It turned out that this was the case for aggregates, which were tracked for at least 80 s. It should be kept in mind that this is a selection effect towards slow moving particles. Also the component in the z direction was not measurable due to the larger error of the distance determination compared to the CCD position. The x and y components are shown in Fig. 8 (bottom). The numbers are generally small, i.e. below 0.3 mm s^{-2} in the maximum. The acceleration in the direction of the spacecraft motion (blue line) is virtually zero, only two aggregates have a significant negative acceleration. In contrast to that, the a_x component shows a wider spread and all but three aggregates have a negative acceleration. Negative in a_x again means down in Fig. 1, which is away from the sun. We did a visual correlation check of all aggregates (including shorter tracks) and can state that the acceleration is correlated neither with the aggregates' sizes nor with their distances to the spacecraft.

4 DISCUSSION

4.1 Interpretation of acceleration

In Section 3.2, we have presented the measured acceleration of dust aggregates in the image-plane projection, which is directed away from the sun for 18 out of 23 aggregates. Another two aggregates had a strong acceleration in $-y$, i.e. perpendicular to that direction. From this, we conclude that we have a directed force and try to provide a qualitative explanation for the outliers.

In this context, it is interesting to take a look at the experiments of von Borstel & Blum (2012). The authors studied the effect of photophoresis (force due to insolation heating and gas interaction) on dust aggregates of the same sizes as found in our work. While the photophoretic force is clearly directed away from the light source, they saw a large fraction of particles (typically ~ 30 per cent) moving in the opposite direction. They qualitatively explain this phenomenon with morphology and rotation of the small, irregular aggregates. The driving force in our case is certainly not photophoresis (because of the lack of gas pressure) but this illustrates how similar forces can act in opposite directions for small particles.

In the following, we aim to interpret the force acting on the 18 aggregates accelerated in the anti-sun-ward direction. A universal force is the radiation pressure, which will be quantified in Section 4.1.1. This force alone is not enough and an additional rocket force from ice sublimation is discussed in Section 4.1.2, from which we derive a lower limit for the aggregates' ice fraction. The possible interaction of charged particles with *Rosetta*'s electric field is discussed in Section 4.1.3.

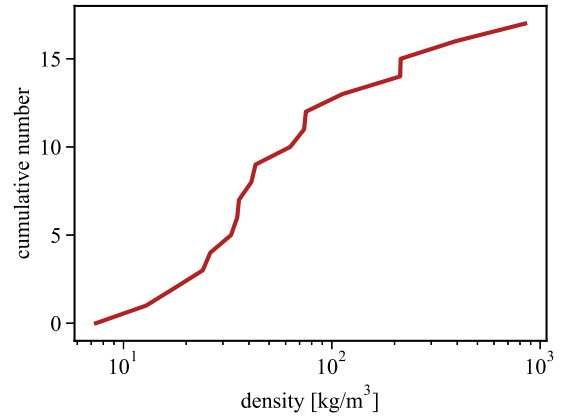


Figure 9. Density distribution derived after equation (4). This requires that radiation pressure is the only acting force, which is likely not the case.

4.1.1 Radiation pressure

The radiation pressure from the impact of solar photons acting on spherical dust aggregates with radius a and density ρ is given by

$$\ddot{x}_{\text{rad}} = -\frac{3I_{\odot}}{4ca\rho r_h^2}, \quad (4)$$

where $I_{\odot} = 1.36 \text{ kW m}^{-2}$ is the solar constant, c is the speed of light and $r_h = 1.48 \text{ au}$ (without unit in equation 4) is the heliocentric distance. For simplicity, we assumed a pressure efficiency of unity, which is a reasonable assumption for dark aggregates. If we wanted to explain the measured acceleration of the dust aggregates purely by radiation pressure ($\ddot{x}_{\text{rad}} = \ddot{x}_{\text{measured}}$), equation (4) has only one free parameter, which is the dust aggregate's mass density.

We solved equation (4) for the density and plot the distribution of resulting densities in Fig. 9. One can see that the range of required densities is very broad, which is in itself speaking against radiation pressure as the only acting force.

4.1.2 Rocket force

An additional force, which can explain the accelerations is the rocket effect from sublimating ice. This was observed for larger aggregates in the coma of comet 103P/Hartley 2 (Kelley et al. 2013) as well as for aggregates close to the comet limb on 67P (Agarwal et al. 2016). The acceleration from this effect (cp. Kelley et al. 2013) is

$$\ddot{x}_{\text{rocket}} = \frac{3m_{\text{H}_2\text{O}}Zv_{\text{th}}f_{\text{ice}}}{4\rho a}. \quad (5)$$

We measured the aggregate radius a and its acceleration \ddot{x} , we know the mass of an H_2O molecule ($m_{\text{H}_2\text{O}} = 3 \times 10^{-26} \text{ kg}$), and we can make a good assumption on the gas thermal velocity $v_{\text{th}} = 500 \text{ m s}^{-1}$ and the aggregates' bulk density $\rho = 1000 \text{ kg m}^{-3}$. We are thus left with two unknown parameters, which are the aggregate's ice fraction f_{ice} and the sublimation rate Z .

It is illustrative to estimate the sublimation rate and derive the ice fraction of the aggregates. We take the energy balance

$$\frac{L}{N_A} \times Z = \frac{(1 - A_B) \times I_{\odot}}{r_h^2}, \quad (6)$$

where $L = 51000 \text{ J mol}^{-1}$ is the latent heat of water ice, N_A is the Avogadro constant and $A_B = 0.0157$ the Bond albedo (Fornasier et al. 2015, at 649 nm). This balance is based on the assumption that the temperature is controlled by the sublimation of water ice

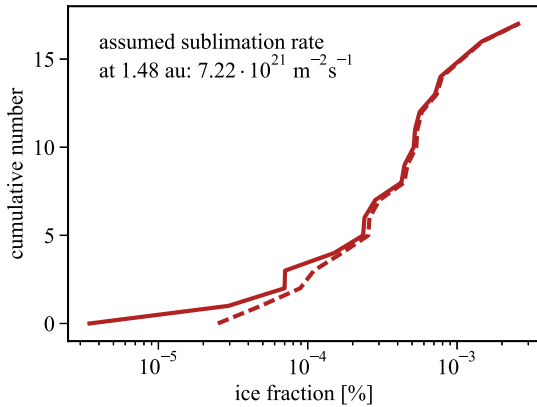


Figure 10. Ice fraction from rocket force after Kelley et al. (2013), assuming a sublimation rate of $7.2 \times 10^{21} \text{ m}^{-2} \text{ s}^{-1}$.

and not radiative cooling (σT^4 term) and results in a sublimation rate of $7.2 \times 10^{21} \text{ m}^{-2} \text{ s}^{-1}$. Also we do not consider the distribution of illumination incidence angles for the warm-up of the aggregate in the right term, such that the derived value for the sublimation rate should be considered an upper limit.

Using this sublimation rate in equation (5), we derive the ice fraction f_{ice} for each particle and plot the distribution in Fig. 10 (dashed line). Using an acceleration, which is reduced by the acceleration explained by radiation pressure (equation 4), we arrive at the red solid line. Ice fractions range from 3×10^{-6} to 2×10^{-3} , which is small compared to the dust-to-ice ratio of ~ 0.2 derived globally (Rotundi et al. 2015). We should keep in mind that the aggregates have lost volatiles during the 200 km journey from the comet to the *Rosetta* spacecraft. Moreover, we have used an upper limit estimate for the sublimation rate, which provides a lower limit on the ice fraction. Also any possible rotation of aggregates would reduce (or re-direct) the observed acceleration and lead to an underestimated ice fraction.

A sophisticated model for the sublimation of millimetre-sized dust pebbles might further constrain the ice fraction but this is beyond the scope of this paper. Overall however, the rocket force gives a better explanation than radiation pressure alone. The difference between the solid and the dashed curve in Fig. 10 shows that radiation pressure acts on those aggregates with the smallest accelerations (smallest ice fractions) and is insignificant for those with a large acceleration.

4.1.3 Charged dust aggregates

Dust aggregates are certainly charged and the spacecraft is known to have a negative potential of -10 V (Nilsson et al. 2015). The interaction of charged particles with the *Rosetta* spacecraft was discussed by Fulle et al. (2015). Within their assumptions, particles smaller than $80 \mu\text{m}$ and with a charge-to-mass ratio that requires densities of 1 kg m^{-3} are significantly affected by *Rosetta*'s electric field. Our particles are too large to expect a measurable acceleration within reasonable assumptions.

However, the main argument why we dismiss charge effects to explain the observed acceleration are our own observations. The shape of the particles' trajectories can be fitted with a constant acceleration. All particles with a measurable acceleration and long trajectory ($> 80 \text{ s}$, see above) change their distance to the spacecraft by a factor of two to five over the observed period. As *Rosetta*'s elec-

tric field must drop with distance, accelerations from electrostatic forces must change accordingly instead of appearing constant.

Further possible effects of charging – even if not visible in the acceleration – will be discussed below in Section 4.2.3.

4.2 Overall picture

To draw a wider conclusion, we first summarize the findings to this point:

- (i) aggregate sizes approx. millimetre
- (ii) number density factor 10 higher than expected
- (iii) number density decreasing with distance to spacecraft
- (iv) number density strongly fluctuating
- (v) v_x and v_y small in spacecraft reference frame
- (vi) v_x small and anti-sun-ward
- (vii) v_z away from spacecraft
- (viii) constant, anti-sun-ward acceleration

We will try to explain these findings with the following scenarios, which are ordered according to likelihood, where we prefer scenario 1.

4.2.1 Scenario 1: Impacts

A scenario that could explain most of these findings are dust aggregates colliding with the spacecraft. If a millimetre to centimetre aggregate would collide with the spacecraft at a velocity of a few m s^{-1} (Fulle et al. 2016), it would likely fragment. According to the collision model compiled by Güttler et al. (2010, also see their fig. 2 for an illustration of the fragmentation process), the fragmentation velocity for porous aggregates made of SiO_2 monomers are around 1 m s^{-1} . These fragments typically contain 80–90 per cent of the parent aggregate's mass (Kothe, Güttler & Blum 2010) and have a rebound velocity, which is orders of magnitude smaller than the impact velocity (Wurm et al. 2005a,b). All this is relative to the system's centre of mass (*Rosetta* in our case), so the aggregates' velocities would be expected to be small in the spacecraft reference frame, which is consistent with our observations. We would have an additional bias towards seeing slow fragments as fast particles would be gone fast. The negative v_x values are consistent with an impact on the spacecraft body, which is above the image in the representation of Fig. 1.

The two to three bursts we see could then be explained by two to three parent particles impacting the spacecraft. The total volume of fragments we studied would require three parent aggregates of 12 mm diameter each, assuming we see all fragments, which is certainly not the case. Assuming a large global production rate of 1.1×10^5 centimetre-sized particles per second from one cometary hemisphere (Fulle et al. 2016, table 7), 4.4×10^{-7} particles cross a square metre per second at *Rosetta*'s comet distance of 200 km. The chance of having a single impact of a 12 mm aggregate for the full duration of 130 min is thus 3 per cent. Three of these collisions would be even less likely but in the dynamic cometary environment with jets and outbursts these can certainly not be excluded. Also, as stated above, the amount of dust in this sequence is very high compared to other observation activities with similar geometry, and large variations in dust collection are reported by the three *in situ* dust instruments.

Another possibility to address the low impact probability is the size of the aggregates. The aggregates could have been smaller than expected if their reflectance is higher than predicted by equation (2). This could be the case in the presence of interior water ice revealed

after breakup. In that case, the required parent aggregate would be accordingly smaller, implying a higher flux and thus collision probability.

4.2.2 Scenario 2: Dust ablating from Rosetta

An alternative explanation for aggregates that are slow and directed away from *Rosetta* is the ablation of a dust layer on the spacecraft's z panel (normal to the camera viewing vector towards $+z_{S/C}$). A typical attitude of *Rosetta* is with the boresight and thus the z panel directed towards the comet most of the time. The orbit at the time of observation was at a phase angle of 90° so that the z panel would not be exposed to direct sunlight. At the beginning of the studied activity, *Rosetta* was rotated towards the sun such that the z panel was illuminated at a flat incidence angle of 75° . It is reasonable to assume that the z panel was covered with dust in a similar fashion as the COSIMA targets (Langevin et al. 2016; Ellerbroek et al., 2017). The spacecraft body is exposed for a much longer time than individual COSIMA targets and although the spacecraft MLI foil's interaction with dust are not well known it is expected that dust would stick to these in a similar fashion.

The open question to this scenario is the process of ablation. The surface of the spacecraft body is cold and dust that might have kept volatiles on the way from the comet to the spacecraft could retain those also while resting on the z panel. These volatiles might be able to lift the dust when exposed to the sun. It is at least thinkable that these can produce showers as observed, as the ablation of the first chunk is changing the shadowing and thermal properties of the neighbouring material. Unfortunately, the process of dust lift-off against the van der Waals force is uncertain, in particular if the dust is compacted during deposition (Blum et al. 2014). We therefore cannot further elaborate on this scenario but consider it as overall realistic.

4.2.3 Scenario 3: Charge disruption

Aiming to explain showers of dust detection in the GIADA GDS sensor (laser curtain), Fulle et al. (2015) described the possibility of particle breakup due to electric charging. Following the charging of aggregates from numerical simulations of Auer, Kempf & Gruen (2007), they concluded that aggregates could break up in the spacecraft's electric field if they are extremely fluffy, i.e. if they collect more charge than a sphere while at the same time having a smaller cohesive strength. They also estimate the deceleration of aggregates approaching the spacecraft, which would imply the possibility to deflect particles with large enough charge-to-mass ratio. Charge breakup can explain the GIADA showers, and one fractal particle has possibly been observed with MIDAS (Mannel et al. 2016).

Following the calculations of Fulle et al. (2015), we should expect neither the breakup of centimetre-sized parent aggregates nor a strong enough deflection of millimetre-sized aggregates. This model is therefore not expected to explain our findings, supported by the following observations: (i) Among 109 aggregates in our field of view, we have not seen a single aggregate breaking up. (ii) Also among all the aggregates where the acceleration could be determined, we have not seen a single trajectory with a non-constant acceleration. (iii) We do not see a correlation between the aggregates' acceleration and their distance to the spacecraft, which would be the case in an electric field.

Overall, electric forces might be in place but too small for us to measure.

5 CONCLUSION

We have characterized 109 aggregates, which were found to be close to the spacecraft, in the field of view of the OSIRIS WAC. We were able to determine their sizes and velocities and, for a subset of 23 aggregates, their accelerations. We concluded that the aggregates must have interacted with the spacecraft in order to explain their small velocities, which are directed away from *Rosetta*. The accelerations were directed away from the sun and can be explained with a rocket force, which constrains their ice fraction to be above 10^{-5} to 10^{-3} for different aggregates. For the initial interaction, we describe three scenarios. None of them works to the full satisfaction explaining all observations but the likeliest scenario is a collisional interaction described in Section 4.2.1.

ACKNOWLEDGEMENTS

OSIRIS was built by a consortium led by the Max-Planck-Institut für Sonnensystemforschung, Göttingen, Germany, in collaboration with CISAS, University of Padova, Italy, the Laboratoire d'Astrophysique de Marseille, France, the Instituto de Astrofísica de Andalucía, CSIC, Granada, Spain, the Scientific Support Office of the European Space Agency, Noordwijk, The Netherlands, the Instituto Nacional de Técnica Aeroespacial, Madrid, Spain, the Universidad Politécnica de Madrid, Spain, the Department of Physics and Astronomy of Uppsala University, Sweden, and the Institut für Datentechnik und Kommunikationsnetze der Technischen Universität Braunschweig, Germany. The support of the national funding agencies of Germany (DLR), France (CNES), Italy (ASI), Spain (MEC), Sweden (SNSB) and the ESA Technical Directorate is gratefully acknowledged. We thank the *Rosetta* Science Ground Segment at ESAC, the *Rosetta* Mission Operations Centre at ESOC and the *Rosetta* Project at ESTEC for their outstanding work enabling the science return of the *Rosetta* Mission.

YL was partially supported by grant nos. 017/2014/A1 and 039/2013/A2 of FDCT, Macau.

REFERENCES

- Agarwal J. et al., 2016, MNRAS, 462, S78
 Auer S., Kempf S., Gruen E., 2007, in Krueger H., Graps A., eds, EAS Publ. Ser. Vol. 643, Workshop Dust Planet. Syst., Computed Electric Charges of Grains with Highly Irregular Shapes. ESA, Noordwijk, p. 177
 Bentley M. S. et al., 2016, Nature, 537, 73
 Blum J., Gundlach B., Mühle S., Trigo-Rodríguez J. M., 2014, Icarus, 235, 156
 Ellerbroek L. E. et al., 2017, MNRAS, 469, S204
 Fornasier S. et al., 2015, A&A, 583, A30
 Fulle M. et al., 2015, ApJ, 802, L12
 Fulle M. et al., 2016, ApJ, 821, 19
 Güttler C., Blum J., Zsom A., Ormel C. W., Dullemond C. P., 2010, A&A, 513, A56
 Hansen K. C. et al., 2016, MNRAS, 462, S491
 Jorda L., Spjuth S., Keller H. U., Lamy P., Llebaria A., 2010, in Bouman C. A., Pollak I., Wolfe P. J., eds, Proc. SPIE Conf. Ser. Vol. 7533, Computational Imaging VIII. SPIE, Bellingham, p. 753311
 Jorda L. et al., 2016, Icarus, 277, 257
 Keller H. U. et al., 2007, Space Sci. Rev., 128, 433
 Kelley M. S., Lindler D. J., Bodewits D., A'Hearn M. F., Lisse C. M., Kolokolova L., Kissel J., Hermalyn B., 2013, Icarus, 222, 634
 Kothe S., Güttler C., Blum J., 2010, ApJ, 725, 1242
 Langevin Y. et al., 2016, Icarus, 271, 76
 Mannel T., Bentley M. S., Schmied R., Jeszenszky H., Levasseur-Regourd A. C., Romstedt J., Torkar K., 2016, MNRAS, 462, S304

Nilsson H. et al., 2015, *A&A*, 583, A20
 Ott T. et al., 2017, *MNRAS*, 469, S276
 Rotundi A. et al., 2015, *Science*, 347, 3905
 Tubiana C. et al., 2015, *A&A*, 583, A46
 von Borstel I., Blum J., 2012, *A&A*, 548, A96
 Wurm G., Paraskov G., Krauss O., 2005a, *Phys. Rev. E*, 71, 021304
 Wurm G., Paraskov G., Krauss O., 2005b, *Icarus*, 178, 253

APPENDIX A: PHASE FUNCTION

We used OSIRIS NAC images in the orange filter for this study, focusing on observations with high phase angles ($>60^\circ$). For comparability to Fornasier et al. (2015), we constrained the study to observations in the year 2014, which turned out to be concentrated at specific areas of the surface or over the limb. Using the last version of Spice kernels and the SPC SHAP8 v1.8 shape model (Jorda et al. 2016), we simulated rendered images with same observational conditions in the OASIS tool (Jorda et al. 2010). From the rendered images, we estimate the photometric distribution of the active pixels and then calculated the standard deviation. All pixels under the condition

$$R_{\text{pixel}} > R_{\text{image,mean}} \times \left(1 - \frac{R_{\text{rendered,stddev}}}{R_{\text{rendered,mean}}}\right) \quad (\text{A1})$$

were then extracted and divided by the total active area (illuminated and shadowed ones). We keep the nomenclature from above that the reflectance (intensity divided by solar flux, taken from OSIRIS level 3B images) is denoted as R . To calculate the reflectance at large phase angles, we divided the data into phase angle bins of 2° and computed the weighted reflectance as

$$R = \frac{\sum A_i \times R_i}{\sum A_i}, \quad (\text{A2})$$

where i is the image index and A_i is the observed active area in this image. Thereby, we equalize the statistical values of R from images taken at closer distance to the nucleus. The result is plotted as the red circles in Fig. 3.

APPENDIX B: DETECTION LIMIT

If the signal of one pixel is ΔR_{min} , the integrated normalized signal $R_{\text{dust,min}}$ of an aggregate with an area of N pixels is given as

$$R_{\text{dust,min}} = \Delta R_{\text{min}} \times N \quad (\text{B1})$$

$$= \Delta R_{\text{min}} \times \pi \times \left(\frac{D}{2}\right)^2 \quad (\text{B2})$$

$$= \Delta R_{\text{min}} \times \frac{\pi}{4} 181^2 \delta^{-1.76} \quad (\text{using equation 1}). \quad (\text{B3})$$

From this, we get the minimal detectable radius a_{min} of an aggregate as

$$a_{\text{min}} = \frac{1}{\sqrt{\pi}} \sqrt{\frac{R_{\text{dust,min}}}{R_{67P}(\alpha)}} \times \frac{13.5 \mu\text{m}}{136 \text{mm}} \times \delta \quad (\text{B4})$$

$$= \frac{1}{\sqrt{\pi}} \sqrt{\frac{\frac{\pi}{4} \Delta R_{\text{min}} 181^2 \delta^{-1.76}}{R_{67P}(\alpha)}} \times \frac{13.5 \mu\text{m}}{136 \text{mm}} \times \delta \quad (\text{B5})$$

$$= \sqrt{\frac{\Delta R_{\text{min}} 90^2}{R_{67P}(\alpha)}} \times \frac{13.5 \mu\text{m}}{136 \text{mm}} \times \delta^{0.12}, \quad (\text{B6})$$

which is only marginally depending on the aggregate distance δ . For ΔR_{min} , we assume 15 digital numbers, which is close to the noise, and translate this into a reflectance.

¹Max Planck Institute for Solar System Research, Justus-von-Liebig-Weg 3, D-37077 Göttingen, Germany

²LESIA, Observatoire de Paris, PSL Research University, CNRS, Univ. Paris Diderot, Sorbonne Paris Cité, UPMC Univ. Paris 06, Sorbonne Universités, 5 place Jules Janssen, F-92195 Meudon, France

³Space Science Institute, Macau University of Science and Technology, Avenida Wai Long, Taipa, Macau

⁴INAF-Osservatorio Astronomico di Trieste, via Tiepolo 11, I-34143 Trieste, Italy

⁵University of Oldenburg, Ammerländer Heerstraße 114, D-26129 Oldenburg, Germany

⁶Center of Studies and Activities for Space (CISAS) ‘G. Colombo’, University of Padova, via Venezia 15, I-35131 Padova, Italy

⁷Department of Physics and Astronomy, University of Padova, Vicolo dell’Osservatorio 3, I-35122 Padova, Italy

⁸Laboratoire d’Astrophysique de Marseille, UMR 7326, CNRS & Aix Marseille Université, F-13388 Marseille Cedex 13, France

⁹Centro de Astrobiología, CSIC-INTA, E-28850 Torrejon de Ardoz, Madrid, Spain

¹⁰International Space Science Institute, Hallerstrasse 6, CH-3012 Bern, Switzerland

¹¹Scientific Support Office, European Space Research and Technology Centre/ESA, Keplerlaan 1, Postbus 299, NL-2201 AZ Noordwijk ZH, the Netherlands

¹²Department of Physics and Astronomy, Uppsala University, Box 516, SE-75120 Uppsala, Sweden

¹³PAS Space Research Center, Bartycka 18A, PL-00716 Warszawa, Poland

¹⁴Department of Astronomy, University of Maryland, College Park, MD 20742-2421, USA

¹⁵LATMOS, CNRS/UVSQ/IPSL, 11 Boulevard d’Alember, F-78280 Guyancourt, France

¹⁶INAF, Osservatorio Astronomico di Padova, Vicolo dell’Osservatorio 5, I-35122 Padova, Italy

¹⁷CNR-IFN UOS Padova LUXOR, Via Trasea 7, I-35131 Padova, Italy

¹⁸Jet Propulsion Laboratory, M/S 183-301, 4800 Oak Grove Drive, Pasadena, CA 91109, USA

¹⁹Department of Industrial Engineering, University of Padova, Via Venezia 1, I-35131 Padova, Italy

²⁰University of Trento, Faculty of Engineering, via Mesiano 77, I-38123 Trento, Italy

²¹Operations Department, European Space Astronomy Centre/ESA, PO Box 78, E-28691 Villanueva de la Cañada (Madrid), Spain

²²Aix Marseille Université, CNRS, LAM (Laboratoire d’Astrophysique de Marseille) UMR 7326, F-13388 Marseille, France

²³Instituto de Astrofísica de Andalucía (CSIC), c/ Glorieta de la Astronomía s/n, E-18008 Granada, Spain

²⁴Deutsches Zentrum für Luft- und Raumfahrt (DLR), Institut für Planetenforschung, Rutherfordstraße 23, D-12489 Berlin, Germany

²⁵Graduate Institute of Astronomy, National Central University, 300 Chung-Da Rd, Chung-Li 32054, Taiwan

²⁶Institut für Geophysik und extraterrestrische Physik, Technische Universität Braunschweig, Mendelssohnstr 3, D-38106 Braunschweig, Germany

²⁷Department of Information Engineering, University of Padova, Via Gradenigo 6/B, I-35131 Padova, Italy

²⁸NASA Ames Research Center, Moffett Field, CA 94035, USA

²⁹Physikalisches Institut der Universität Bern, Sidlerstr 5, CH-3012 Bern, Switzerland

³⁰Center for Space and Habitability, University of Bern, CH-3012 Bern, Switzerland